Journal of Microscopy, Vol. 220, Pt 3 December 2005, pp. 176–189
Received 10 September 2004; accepted 14 September 2005

Studies on depth-of-field effects in microscopy supported by numerical simulations

DARRYL R. OVERBY* & MARK JOHNSON*
Department of Mechanical Engineering, MIT, Cambridge, MA, U.S.A.
**Department of Biomedical Engineering, Northwestern University, Evanston, IL, U.S.A.*

Key words. Convex microscopy, depth-of-field, extracellular matrix, non-interpenetrating, projection, simulation, specific surface area, stereology, volume fraction

Summary

Micrographs are two-dimensional (2D) representations of three-dimensional (3D) objects. When the depth-of-field of a micrograph is comparable with or larger than the characteristic dimension of objects within the micrograph, measured 2D parameters (e.g. particle number density, surface area of particles, fraction of open space) require stereological correction to determine the correct 3D values. Here, we develop a stereological theory using a differential approach to relate the 3D volume fraction and specific surface area to the 2D projected area and perimeter fractions, accounting for the influence of depth-of-field. The stereological theory is appropriate for random isotropic arrangements of non-interpenetrating particles and is valid for convex geometries (e.g. spheres, spheroids, cylinders). These geometrical assumptions allow the stereological formulae to be expressed as a set of algebraic equations incorporating a single parameter to describe particle shape that is tightly bounded between 1.5π and 2π. The stereological theory may also be applied to arrangements of interpenetrating convex particles, and for this case, the resulting stereological formulae become identical to the formulae previously presented by Miles. To test the accuracy of the stereological theory, random computational arrangements of non-interpenetrating and interpenetrating spheres or cylinders are analysed, and the projected area and perimeter fractions are numerically determined as a function of depth-of-field. The computational results show very good agreement with the theoretical predictions over a broad range of depth-of-field, volume fraction and particle geometry for both non-interpenetrating and interpenetrating particles, demonstrating the overall accuracy of the stereological theory. Applications of the stereological theory towards analysis of biological tissues and extracellular matrix are discussed.

Correspondence to: Professor Darryl Overby. Present address: Department of Biomedical Engineering, Tulane University, New Orleans, LA, U.S.A. E-mail: doverby@tulane.edu

Introduction

Scientists and engineers have increasingly focused their attention upon problems at the micrometre and nanometre length scales. At these tiny scales, local heterogeneities and statistical fluctuations take on an increased importance, complicating both theoretical and experimental attempts to determine material properties. A further challenge is the difficulty of making direct measurements of properties and parameters at these tiny scales.

Electron microscopy is a commonly used tool to characterize materials, both biological and otherwise, at nanometre length scales, and is therefore useful for determination of nanoscale material properties. For instance, the permeability of a tissue to fluid flow (the specific hydraulic conductivity) can be estimated from the porosity and surface area of the extracellular matrix (Ethier *et al.*, 1986; Levick, 1987; Overby *et al.*, 2001). The elastic modulus of cells has been estimated by determining the intracellular actin filament density (Satcher & Dewey, 1996; Satcher *et al.*, 1997), and collagen and elastin fibril density could potentially be used to determine the elastic modulus of a connective tissue. Mitochondrial density has been determined to assess metabolic function (Hoang *et al.*, 2002), while quantitative morphological studies have used electron micrographs to determine the surface area of alveoli in the lungs (Weibel, 1973) and hepatocytic membranes in the liver (Bolender *et al.*, 1978), as well as the number of neurons in subdivisions of the hippocampus (West *et al.*, 1991) and the morphological characteristics of collagen fibres in articular cartilage (Långsjö *et al.*, 1999).

Electron microscopy provides a nanoscale view of cell and tissue architecture. However, electron micrographs are inherently two-dimensional (2D) and therefore 2D parameters describing the nanoscale architecture must undergo stereological correction in order to obtain the three-dimensional (3D) parameters that are typically needed to estimate material properties. Stereology is the science of recovering 3D geometric information from lower dimensional images and has been used in a wide variety of fields, ranging from metallurgy

(Karlsson & Cruz-Orive, 1992) to anatomy and physiology (Weibel, 1967; Weibel & Paumgartner, 1978; Baddeley *et al.*, 1986). If the microscopy sections are sufficiently thin, then 2D parameters measured from these images can often be directly related to their 3D counterparts. For example, the 3D parameters we will concentrate on in this study, tissue volume fraction (V_V: volume of the tissue component per total volume) and specific surface (S_V: surface area of tissue component per total volume), can be related to 2D parameters measured from the micrographs, namely the projected area fraction (A'_A: area of the tissue component per total micrograph area) and perimeter fraction (L'_A: perimeter bounding the tissue component per total micrograph area). If A'_A is measured from a random 2D slice through a two-phase 3D material, then (Weibel & Elias, 1967; Underwood, 1970; Weibel & Paumgartner, 1978; Cruz-Orive, 1997):

$$V_V = A'_A \tag{1a}$$

is an unbiased estimate of the volume fraction. If the section orientation is also arbitrary with respect to the orientation of the particles then

$$S_V = (4/\pi)L'_A \tag{1b}$$

yields an unbiased estimate of the specific surface.

Rather than being infinitesimally thin 2D slices, electron micrographs are projections of 3D sections with a finite thickness. Therefore, errors associated with assuming that these projections arise from infinitesimally thin 2D slices in Eq. (1) become increasingly large as the thickness of the section contributing to the projected image (known as the depth-of-field) increases beyond the length scale of interest (such as the size or distance between objects being examined). Ultramicrotomes, for instance, produce sections that are roughly 100 nm in thickness, comparable with the depth-of-field obtained using other processing techniques for electron microscopy, such as quick-freezing/deep-etch (Overby *et al.*, 2001) or ultracryomicroscopy (Dubochet *et al.*, 1988). Thus, imaging analysis at nanometre length scales using electron microscopy necessitates stereological correction to account for depth-of-field effects.

With increasing depth-of-field, more out-of-plane structures contribute to the projected image, increasing the apparent density of the section, and thereby increasing A'_A. This phenomenon, known as overprojection (Abercrombie, 1946; Weibel & Elias, 1967; Underwood, 1970), leads to a second confounding effect whereby projections from individual particles occupy the same location on the projected image and so overlap and obscure one another (Underwood, 1970; Weibel, 1980). Both overprojection and overlap introduce bias into the stereological relationships in Eq. (1), and corrections for these depth-of-field effects are needed to determine V_V and S_V from thick sections. Miles (1976) presented formulae that account for these depth-of-field effects for the case of isotropic and uniform random arrangements of opaque, convex particles that interpenetrate to form not-necessarily convex particle aggregates (Miles, 1976; Weibel & Paumgartner, 1978; Weibel, 1980; Stoyan *et al.*, 1987). These corrections, however, are often difficult to apply in practice because the mathematical formulae are sensitive to the particular geometry of the elemental particles and the solution requires measurement of the projected curvature (Miles, 1976; Weibel, 1980). Therefore, it may be desirable to introduce geometrical simplifications into a stereological theory in order to obtain mathematical formulae that relate V_V and S_V directly in terms of A'_A, L'_A and t (the depth-of-field) (Weibel, 1979).

Here we develop theoretical equations following a differential approach to account for depth-of-field effects and build upon the stereological theory described by Miles (1976). The geometry we consider is a random model in which it is assumed that convex particles are arranged randomly and isotropically (Miles, 1977). The theory developed is equally capable of describing arrangements of non-interpenetrating particles as well as arrangements of interpenetrating particles. The latter geometry was considered by Miles (1976). For both cases, geometrical assumptions are introduced to simplify the stereological formulae so that they may be expressed as algebraic equations that describe the 3D parameters V_V and S_V in terms of the 2D parameters A'_A and L'_A, t, and a single parameter (c) that is tightly bounded between 1.5π and 2π. These geometric assumptions are appropriate for a range of spheroidal and cylindrical geometries.

To validate the stereological theory, the theoretical predictions of A'_A and L'_A are shown to be consistent with numerical results obtained from Monte Carlo simulations of isotropic uniform random arrangements of spheres or cylinders, the latter being representative of the fibrous ultrastructure generally observed within extracellular matrix. Both non-interpenetrating and interpenetrating particles are considered.

Stereological formulation

Consider a large volume in which opaque particles are randomly positioned and isotropically orientated within a transparent space. All particles have a similar shape with a regular convex geometry (e.g. spheres, cylinders), and are distributed in such a way so as not to interpenetrate one another (we will later allow the particles to interpenetrate). Within this volume, consider a rectangular test section of area A_T. We examine the projection of particles onto this planar area from a test volume ($V_T = A_T t$) that extends a distance t (the depth-of-field) orthogonally from the projection plane (Fig. 1A). Our goal is to derive differential equations that describe how the projected area fraction (A'_A) and projected perimeter per unit area (L'_A) change as a function of t.

To find these equations, it is useful to consider the effect on these parameters as the depth-of-field is increased from t to $t + \mathrm{d}t$, as illustrated in Fig. 1(A). As t is increased, A'_A and L'_A both change as the number of particles contributing to the

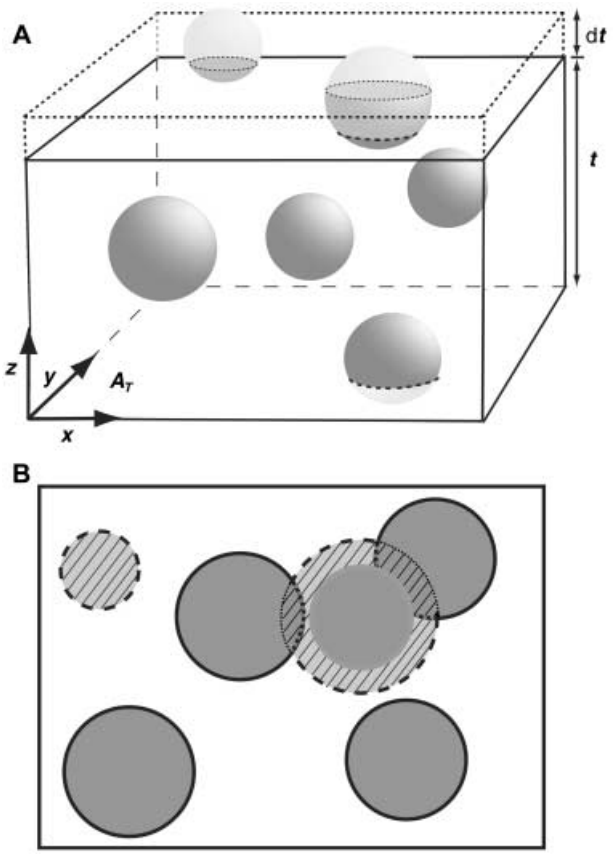

Fig. 1. (A) Schematic of convex particles contained within a rectangular sample volume $V_T = A_T t$, as the depth-of-field is increased from t to $t + \mathrm{d}t$ (dotted lines). Dark grey particles are contained within depth-of-field t and are truncated by either the upper or the lower surfaces of V_T (dashed curves), while light grey particles are contained within the increased depth-of-field $\mathrm{d}t$ and are truncated at $z = t + \mathrm{d}t$ (dotted curves). (B) The projection of the particles contained within V_T as the depth-of-field is increased from t (grey area, black perimeter) to $t + \mathrm{d}t$ (cross-hatched area, dashed perimeter). Both the solid and the dashed perimeter are observed on the projected image, while both the heavily and the lightly dotted perimeter are obscured due to overlap. The lightly dotted perimeter represents the portion of the increased projected perimeter that is obscured by lower-lying particles, while the heavily dotted perimeter represents the portion of projected perimeter of lower-lying particles that is obscured by the increase in projected area. See text for further details.

projected image increases (i.e. overprojection). The derivation, however, is considerably complicated by the overlap effect, whereby projections from individual particles occupy the same position on the projection plane and obscure one another. Figure 1(B) shows the effect of increasing t to $t + \mathrm{d}t$ on the projected image. We first consider how this affects A'_A and then L'_A.

Derivation of the projected area fraction, $\mathrm{A}'_\mathrm{A}(\mathrm{t})$

As depth-of-field increases, more particles are incorporated within V_T, increasing the total area projected by these particles onto the projection plane and thereby increasing A'_A. Neglecting the effect of overlap, the mean projected area of the jth convex particle (averaged over all possible particle orientations), $A'(j)$, can be related to its surface area, $S(j)$, by the Cauchy relationship:

$$A'(j) = \frac{S(j)}{4} \tag{2}$$

where primed symbols indicate 2D projected quantities (Vouk, 1948; Underwood, 1970). To find the total projected area, one must sum the observed contributions from all the particles contained within V_T. However, because of overlap, some portion of $A'(j)$ can be overlapped and obscured on the projected image. Specifically, overlap occurs whenever the projected area of a particle that lies nearer to the bottom of V_T occupies the same position on the projection plane as the projected area of another particle that lies nearer to the top of V_T.

To formulate a differential equation describing how A'_A changes with t, consider the change in total projected area (excluding overlap) as the depth-of-field is increased from t to $t + \mathrm{d}t$. Any change in the total projected area can arise from either an increase in the projected area of individual particles intersected by the upper surface of V_T, or an increase in the total number of particles contained within V_T. If m is the total number of particles contained at least partially within V_T, then the rate of increase of the total projected area (excluding overlap) is given by

$$\frac{\mathrm{d}}{\mathrm{d}t}\sum_{j=1}^{m(t)} A'(j).$$

Now, consider the fraction of this increase in projected area that is overlapped by lower-lying particles within V_T. Figure 1(B) shows the projected area from particles that are contained within depth-of-field t as dark grey, and the increase in projected area that is not overlapped as light grey and cross-hatched. The regions where the increased projected area is overlapped are shown as both dark grey and cross-hatched. This latter area does not contribute to the increase in observed projected area when the depth-of-field increases from t to $t + \mathrm{d}t$.

To account for the overlap effect, the rate of increase in projected area must be multiplied by the probability (f) that this increased projected area does not intersect the projected area of any lower-lying particle. It might seem that f should equal $1 - A'_A$ (the unoccupied area fraction on the projected image), but this does not properly allow for the volumetric exclusivity of non-interpenetrating particles, which requires that the particles be located only within certain regions of 3D space, namely within the void volume $(1 - V_V)A_T\mathrm{d}t$. The assumption of non-interpenetration is enforced by requiring that any newly added projected area be uniformly and randomly distributed within the space that is not already occupied by other particles on the upper surface of V_T. With this constraint, f can be computed as the ratio of (i) the unoccupied area on the projection plane to (ii) the total area available for placement of the increased projected area at the upper surface of V_T. The former

quantity is $(1 - A'_A)A_T$, and the latter is $(1 - V_V)A_T$, yielding $f = (1 - A'_A)/(1 - V_V)$.

The rate of increase in the observed projected area ($A_T \mathrm{d}A'_A/\mathrm{d}t$) can now be expressed as:

$$A_T \frac{\mathrm{d}A'_A}{\mathrm{d}t} = f \frac{\mathrm{d}}{\mathrm{d}t} \sum_{j=1}^{m(t)} A'(j) = \left(\frac{1 - A'_A}{1 - V_V} \right) \frac{\mathrm{d}}{\mathrm{d}t} \sum_{j=1}^{m(t)} A'(j). \quad (3)$$

Using the Cauchy relationship (Eq. 2), the mean projected area of each particle can be related to its surface area yielding:

$$A_T \frac{\mathrm{d}A'_A}{\mathrm{d}t} = \left(\frac{1 - A'_A}{4(1 - V_V)} \right) \frac{\mathrm{d}}{\mathrm{d}t} \sum_{j=1}^{m(t)} S(j). \quad (4)$$

The summation represents the total surface area of all m particles contained within V_T. Defining S_V as the surface area per unit volume, the total surface area in V_T is $S_V A_T t$, and therefore

$$\frac{\mathrm{d}A'_A}{\mathrm{d}t} = \left(\frac{1 - A'_A}{1 - V_V} \right) \frac{S_V}{4}. \quad (5)$$

Equation (5) is the differential equation describing the change in the projected area fraction with depth-of-field. This equation must be solved using the initial condition from Eq. (1) that $A'_A = V_V$ at $t = 0$ [also known as the Delesse condition (Weibel & Elias, 1967; Underwood, 1970; Cruz-Orive, 1997)]. The resulting stereological relationship describes $A'_A(t)$ for non-interpenetrating particles:

$$A'_A = 1 - (1 - V_V) \exp\left[\frac{-S_V t}{4(1 - V_V)} \right]. \quad (6)$$

Recognizing that $4(1 - V_V)/S_V$ represents the mean separation distance between particles (Underwood, 1970) or the hydraulic diameter of a porous medium (Happel & Brenner, 1983) allows a dimensionless depth-of-field to be defined as $\tau = t S_V/4(1 - V_V)$. Then,

$$\frac{1 - A'_A}{1 - V_V} = \exp[-\tau]. \quad (7)$$

This relationship indicates that the normalized projected void area fraction is a monotonically decreasing function that depends solely upon the dimensionless ratio of the depth-of-field to the mean separation distance between particles, as shown by the solid line in Fig. 2(A).

Miles (1976) considered the case of interpenetrating particles for which $f = (1 - A'_A)$ (as the particles can be placed anywhere along the upper surface of V_T, regardless of volume exclusivity). For this case, due to particle interpenetration, the total surface area of all individual particles is not equal to the total surface area of the interpenetrating particle aggregates. The appropriate relationship between $S(j)$ and S_V for interpenetrating particles has been shown to be (Miles, 1976):

$$\sum_{j=1}^{m(t)} S(j) = \frac{S_V A_T t}{1 - V_V}. \quad (8)$$

Using this relationship in Eq. (4) and replacing f with $(1 - A'_A)$ yields an equation describing the projected area fraction for

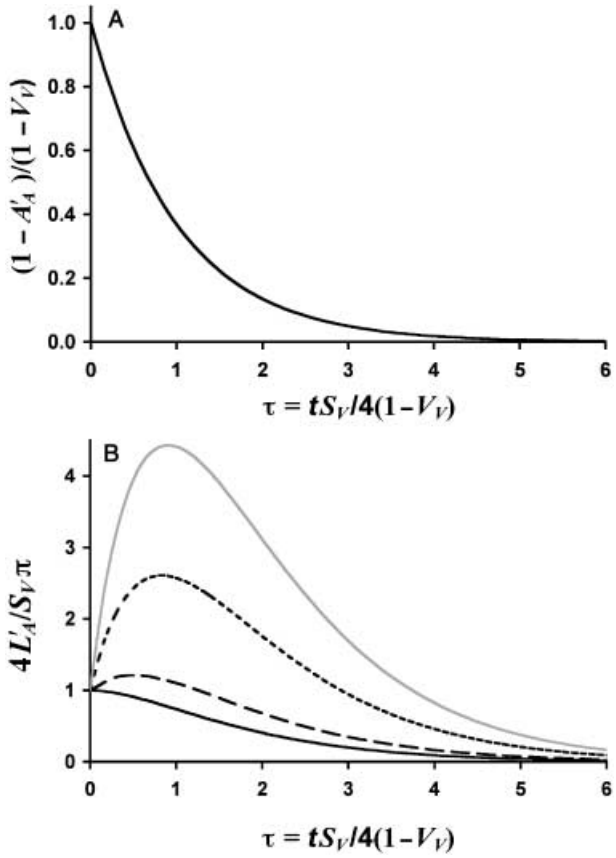

Fig. 2. Theoretical predictions of (A) the dimensionless void area fraction $(1 - A'_A)/(1 - V_V)$ and (B) the dimensionless perimeter fraction $4L'_A/S_V\pi$ given by Eqs (7) and (11) as a function of the dimensionless depth-of-field ($\tau = tS_V/4(1 - V_V)$). For panel B, $\beta = 4(1 - V_V)/cV_V = 0$ (solid black curve), $\beta = 1$ (dashed curve), $\beta = 5$ (dotted curve) or $\beta = 10$ (grey curve).

interpenetrating particles as a function of depth-of-field that, interestingly, is identical to that shown in Eq. (6) (Stoyan *et al.*, 1987). Thus, the loss of surface area due to particle interpenetration is exactly analogous to the loss of projected area due to overlap.

Derivation of the projected perimeter fraction, $L'_A(t)$

Increasing depth-of-field has two competing effects upon the projected perimeter. First, similar to the situation considered for A'_A, increasing t incorporates additional projected perimeter, the non-overlapped portion of which acts to increase L'_A (represented by the dashed perimeter on Fig. 1B). Second, unlike the case for A'_A, the accompanying increase in projected area overlaps and obscures some portion of L'_A that was observed prior to the increase in t (represented by the heavily dotted perimeter on Fig. 1B).

The increase in projected perimeter due to the first effect is directly analogous to the increase in projected area considered in the previous section (Eq. 3), such that the rate of increase of L'_A can be expressed as:

$$\frac{f}{A_T}\frac{\mathrm{d}}{\mathrm{d}t}\sum_{j=1}^{m(t)}L'(j)$$

where $L'(j)$ is the total projected perimeter of the jth particle, excluding the effects of overlap.

Accounting for the second phenomenon, namely the decrease in L'_A caused by overlap of projected perimeter by the increase in projected area, is somewhat more complicated. If the increase in projected area at the upper surface of V_T overlaps the projected perimeter of a lower-lying particle, then a portion of this perimeter will be obscured. An illustration of this effect is represented by the heavily dotted perimeter in Fig. 1(B). However, this type of overlap can occur only for that portion of the observed projected perimeter that arises from those aspects of particles that are not intersected by the upper surface of V_T (e.g. those particles with only dark grey in their interiors in Fig. 1B). This is a consequence of the non-interpenetration condition that requires the intersected area of all particles by the upper surface of V_T (or any plane for that matter) to remain mutually exclusive.

Defining $g(L'_A)$ as that portion of L'_A that is susceptible to being overlapped by the increase in projected area, then $g(L'_A)$ is equal to L'_A minus the observed projected perimeter arising from the intersection of particles by the upper surface of V_T. The intersected perimeter with any arbitrary plane is expected to be $\pi S_V/4$ (see Eq. 1). However, due to overlap, only $f\pi S_V/4$ will be observed on the projected image so that $g(L'_A) = L'_A - f\pi S_V/4$, where $f = (1 - A'_A)/(1 - V_V)$. Note that for the case of interpenetrating particles as considered by Miles (1976), $g(L'_A) = L'_A$.

The rate of decrease in $g(L'_A)$ due to overlap by the increase in projected area is computed by assuming that both $g(L'_A)$ and the differential increase in projected area are independently and randomly distributed within the void area $(1 - V_V)A_T$ along the upper surface of V_T. This is because the non-interpenetration condition requires that the increased projected area be positioned within the void area that is not already occupied by other particles, and in order for $g(L'_A)$ to have been previously observed, $g(L'_A)$ must have been located within the same void area on the upper surface of V_T. The rate of decrease in the projected perimeter of lower-lying particles due to overlap is therefore found to be:

$$g(L'_A)\frac{\dfrac{\mathrm{d}}{\mathrm{d}t}\displaystyle\sum_{j=1}^{m(t)}A'(j)}{(1 - V_V)A_T}.$$

Combining this result with the first effect describing the increase in the observed perimeter fraction reveals:

$$\frac{\mathrm{d}L'_A}{\mathrm{d}t} = \frac{f}{A_T}\frac{\mathrm{d}}{\mathrm{d}t}\sum_{j=1}^{m(t)}L'(j) - g(L'_A)\frac{\dfrac{\mathrm{d}}{\mathrm{d}t}\displaystyle\sum_{j=1}^{m(t)}A'(j)}{(1 - V_V)A_T}$$

or

$$\frac{\mathrm{d}L'_A}{\mathrm{d}t} = \frac{(1 - A'_A)}{(1 - V_V)A_T}\frac{\mathrm{d}}{\mathrm{d}t}\sum_{j=1}^{m(t)}L'(j) - \left(L'_A - \frac{(1 - A'_A)S_V\pi}{(1 - V_V)\,4}\right)\frac{\dfrac{\mathrm{d}}{\mathrm{d}t}\displaystyle\sum_{j=1}^{m(t)}A'(j)}{(1 - V_V)A_T}.$$

To simply this relationship, the Cauchy relationship can be used to relate the surface area of a convex particle to its projected area (as done above for the case of A'_A). However, to complete the formulation, the projected perimeter $L'(j)$ must be related to the projected area $A'(j)$. This is done by introducing the mean chord length of the projected particles (Underwood, 1970),

$$\bar{L}'_2 = \pi\sum_{j=1}^{m(t)}A'(j)\Big/\sum_{j=1}^{m(t)}L'(j);$$

note that $A'(j)$ and $L'(j)$ are the non-overlapped area and perimeter projections of the jth particle, respectively. Then, the rate of change of projected perimeter can be expressed as:

$$\frac{\mathrm{d}L'_A}{\mathrm{d}t} = \frac{\pi(1 - A'_A)}{(1 - V_V)\bar{L}'_2A_T}\frac{\mathrm{d}}{\mathrm{d}t}\sum_{j=1}^{m(t)}A'(j) - \left(L'_A - \frac{(1 - A'_A)S_V\pi}{(1 - V_V)\,4}\right)\frac{\dfrac{\mathrm{d}}{\mathrm{d}t}\displaystyle\sum_{j=1}^{m(t)}A'(j)}{(1 - V_V)A_T}.$$

Using the Cauchy relationship to relate $A'(j)$ to $S(j)$ as done for the case of A'_A, yields:

$$\frac{\mathrm{d}L'_A}{\mathrm{d}t} = \frac{S_V\pi}{4}\left(\frac{1}{\bar{L}'_2} + \frac{S_V}{4(1 - V_V)}\right)\left(\frac{1 - A'_A}{1 - V_V}\right) - \frac{S_V}{4(1 - V_V)}L'_A. \quad (9)$$

Imposing the initial condition from Eq. (1b) that $L'_A = \pi S_V/4$ at $t = 0$, Eq. (9) can be solved to find that for non-interpenetrating convex particles:

$$L'_A = \frac{S_V\pi}{4}\left(1 + (\beta + 1)\frac{S_Vt}{4(1 - V_V)}\right)\exp\left[\frac{-S_Vt}{4(1 - V_V)}\right] \quad (10)$$

where

$$\beta = 4(1 - V_V)/(S_V\bar{L}'_2)$$

(the ratio of the mean interparticle spacing to the mean projected chord length). Expressing Eq. (10) in terms of the dimensionless depth-of-field, τ, reveals:

$$\frac{4L'_A}{S_V\pi} = (1 + (\beta + 1)\tau)\exp[-\tau], \quad (11)$$

which is shown by the curves on Fig. 2(B). Unlike the monotonic behaviour observed for the case of A'_A (Eq. 7), the dimensionless projected perimeter fraction first increases with increasing τ for τ less than $\beta/(\beta + 1)$, reaches a maximum and then decreases with increasing τ due to the high degree of overlap at larger depth-of-field. The peak value of $4L'_A/(S_V\pi)$ increases monotonically with β, as illustrated in Fig. 2(B).

For the case of interpenetrating particles, the procedure above can be repeated using the conditions that $f = (1 - A'_A)$ and $g(L'_A) = L'_A$ because the increase in projected area is no longer required to be confined within the void area on the

upper surface of V_T. Using the appropriate relationship for S_V (see Eq. 8), the corresponding dimensionless stereological equation for interpenetrating particles becomes:

$$\frac{4L'_A}{S_V\pi} = (1+\beta\tau)\exp[-\tau] \tag{12}$$

which is identical to the relationship presented by Miles (1976) after recognizing that $\overline{L'_2} = \overline{A'}/\overline{M}$ (Underwood, 1970), where $\overline{A'}$ is the mean projected area per particle (excluding overlap) and $\overline{M}$ is the mean caliper diameter as defined by Miles (in eq. 2b of Miles, 1976). Note that Eq. (12), describing L'_A for interpenetrating particles, is quantitatively different from Eq. (11) for non-interpenetrating particles. In the limit of $\beta \gg 1$ where the particle separation distance is much larger than the mean projected chord length (the dilute limit), Eq. (12) becomes equivalent to Eq. (11), demonstrating that the result of the stereological theory for non-interpenetrating particles is identical to the result for interpenetrating particles in the limit of large β, as would be expected.

To add closure to Eqs (6) and (10) and thus allow V_V and S_V to be computed once A'_A, L'_A and t are known, $\overline{L'_2}$ can be expressed in terms of V_V and S_V (Weibel, 1979).

Determination of mean chord length, $\overline{L'_2}$

For non-interpenetrating particles with any fixed particle shape, $\overline{L'_2}$ can be expressed in terms of V_V and S_V according to:

$$\overline{L'_2} = c\frac{V_V}{S_V} \tag{13}$$

where c is a constant that depends upon the shape of the particle (Wicksell, 1925; Weibel & Gomez, 1962; Weibel, 1979; Stoyan *et al.*, 1987; Ohser & Mücklich, 2000). For example, $c = 3\pi/2$ for a perfect sphere and $c = 2\pi$ for a long cylinder. To examine how c varies for a range of convex shapes, consider two simple geometries: (i) a perfect cylinder of length l and diameter D with aspect ratio $\lambda = l/D$ and (ii) a spheroid with polar radius R_P and equatorial radius R_E with aspect ratio $\lambda = R_P/R_E$. These geometries are useful because by varying λ, c can be computed for convex shapes ranging from a disc or oblate spheroid ($\lambda \ll 1$) to a long cylinder or prolate spheroid ($\lambda \gg 1$). Using reported values of $\overline{A'}$ (the average projected area per particle), $\overline{L'}$ (the average projected perimeter per particle), S_V and V_V for non-interpenetrating particles (Mack, 1956; Underwood, 1970), c can be determined from Eq. (13), where $\overline{L'_2} = \pi\overline{A'}/\overline{L'}$ yielding

$$c = \frac{\pi}{\lambda}\frac{(1+2\lambda)^2}{\pi+2\lambda} \tag{14a}$$

for cylinders,

$$c = \frac{3\pi}{4\kappa\lambda}\frac{[\kappa+\lambda^2\sin^{-1}(\kappa/\lambda)]^2}{[\lambda\kappa+\sinh^{-1}\kappa]} \tag{14b}$$

for prolate spheroids with $\lambda > 1$, and

$$c = \frac{3\pi}{16\kappa\lambda}\frac{\left[2\kappa+\lambda^2\ln\left(\frac{1+\kappa}{1-\kappa}\right)\right]^2}{[\lambda\kappa+\sin^{-1}\kappa]} \tag{14c}$$

for oblate spheroids with $\lambda < 1$, where $\kappa = (|1-\lambda^2|)^{1/2}$ (Overby, 2002).

Figure 3 shows c for cylinders (grey curve, Eq. 14a) and prolate and oblate spheroids (black curve, Eqs 14b and 14c) as a function of λ. These data reveal that tight limits may be placed upon c if particle geometries can be confined within a range of spheroidal or cylindrical geometries:

$$3\pi/2 \le c \le 2\pi. \tag{15}$$

The limits given by Eq. (15) encompass all cylindrical shapes with $\lambda > 0.436$ and all spheroidal shapes with an aspect ratio greater than 3-to-1 ($\lambda > 0.334$). For small λ, c increases beyond 2π for both cylinders and oblate spheroids because of the inverse relationship between c and particle volume (Eq. 13) that rapidly approaches zero for decreasing λ.

Assumptions and limitations

Equations (13) and (15), when combined with Eqs (7) and (11) (non-interpenetrating particles) or Eq. (12) (interpenetrating particles), are a set of algebraic expressions describing A'_A and L'_A explicitly in terms of V_V, S_V, t and a tightly bounded constant (c). Importantly, these formulations allow upper and lower bounds on V_V and S_V to be calculated for a given depth-of-field once A'_A and L'_A have been measured on a 2D micrograph. Under the assumptions of Eq. (15), the stereological formulae reduce to simplified versions of the Miles formulae for the interpenetrating case but do not require the difficult measurement of projected curvature. These simplified formulae may therefore be useful for practising stereologists.

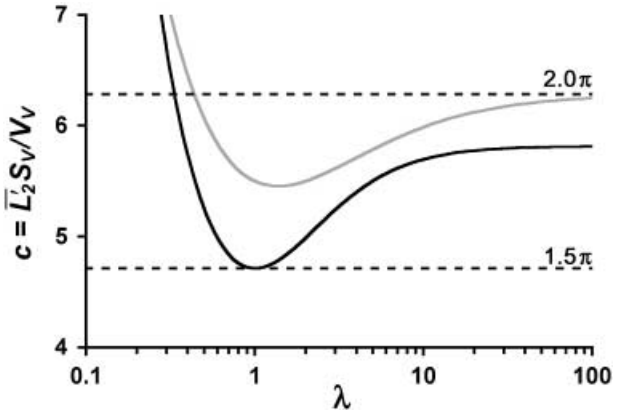

Fig. 3. The value of c (Eq. 14) for generalized cylinders (grey curve) with varying aspect ratio $\lambda = l/D$ (length to diameter) or spheroids (black curve) with varying aspect ratio $\lambda = R_P/R_E$ (polar radius to equatorial radius). The dotted lines represent the limits given by a perfect sphere (1.5π) and a long cylinder (2π); see text for details.

However, before these stereological formulae can be applied in practice, it is important to appreciate the inherent geometrical assumptions underlying Eq. (15) as well as the assumption of an isotropic uniform random particle distribution. A divergence from these assumptions in practice would necessarily lead to a reduced accuracy in the predicted values of V_V and S_V. In essence, the current stereological formulation involves a compromise that accepts a limitation on geometrical variability in exchange for stereological formulae that express V_V and S_V as explicit mathematical functions of A'_A, L'_A and t.

Numerical methods

To investigate the validity of the stereological theory, random computational arrangements of non-interpenetrating spheres and cylinders with known values of V_V and S_V were constructed and analysed to measure A'_A and L'_A as a function of depth-of-field (t), and these results were compared with the predictions from the stereological theory. We also generated arrangements of composite particles made of interpenetrating spheres or cylinders to investigate the performance of the stereological theory for arrangements of non-convex particle shapes. Composite particles made of interpenetrating cylinders arranged end to end as a model of polymer chains were also investigated. For brevity, we do not include the latter methods or results here but refer the interested reader to the thesis by Overby (2002). We consider particle concentrations up to a maximum V_V of 0.2 for spheres and 0.1 for cylinders. Higher concentrations are not considered owing to excluded volume interactions that can give rise to non-random packing arrangements as the random close packing limit ($V_V \approx 0.64$ for spheres) is approached (Donev *et al.*, 2004).

Arrangements of spheres were constructed by random sequential addition (Stoyan *et al.*, 1987; Stoyan, 2000) of individual spheres within a large rectangular volume (V) until a desired volume fraction V_V was attained, where V_V was varied between 0.05 and 0.20. Herczynski (1975) has shown that random sequential addition of spheres gives particle distributions that are indistinguishable from a random Poisson distribution for volume fractions less than 0.22. The diameter (D) of the spheres was constant in some simulations, whereas in others the diameters of the spheres were chosen from a normally distributed random distribution with mean μ_D and standard deviation σ_D, where $\sigma_D/\mu_D = 25\%$. The centroid of each sphere was assigned according to a uniform random distribution within V. Interpenetration was detected if the distance between the newly assigned centroid and any previously assigned centroid was less than the sum of the corresponding sphere radii. The position of each interpenetrating sphere was re-assigned until a non-interpenetrating position was found. Finally, V_V and S_V were computed as the sum over all of the spheres of the volumes and surface areas, respectively, divided by V.

Arrangements of cylinders were constructed by random sequential addition of individual cylinders of diameter D and length l within a large rectangular volume V until a desired volume fraction V_V was attained, where V_V was varied between 0.025 and 0.10. The position and orientation of each cylinder were assigned according to a uniform isotropic distribution (see below), and cylinders were not allowed to interpenetrate. The diameter (D) of each cylinder was assigned to be either a fixed value or a normally distributed random value with mean μ_D and standard deviation σ_D, where $\sigma_D/\mu_D = 25\%$, and the length of each cylinder was varied between $2D$ and $50D$ (uniform for any particular run). The ends of all cylinders were circular and were orientated orthogonal to their centrelines, and cylinders were allowed to extend outside of V (but not included in the determination of V_V, S_V, A'_A or L'_A).

The orientation of each cylinder was defined by two angles: ψ, measured with respect to the vertical axis, and θ, measured with respect to an orthogonal axis contained within the projection plane. θ was assigned as a uniform random number distributed between 0 and 2π, and ψ was assigned between 0 and π according to $\cos^{-1}(1 - 2U)$, where U is a uniform random number between 0 and 1. This distribution produces an isotropic arrangement of cylinders (Ethier, 1983).

The position of the cylinder was then determined by randomly selecting a point within V that was not already occupied by another cylinder and assigning this position to correspond to one end of the cylinder's axis. The axis of the cylinder was then extended to length l in the direction described by θ and ψ. The position and orientation of each newly assigned cylinder was checked for interpenetration with all previously assigned cylinders by comparing the minimum distance between any two centrelines with the sum of the corresponding cylinder radii (see Overby, 2002, for details). Any newly added cylinder that was found to interpenetrate with a previously assigned cylinder was re-orientated from the original starting position by choosing new values of θ and ψ until a non-interpenetrating orientation was found. To avoid an infinite number of iterations, a new starting position for the cylinder's axis was chosen after 50 000 trials if re-orientation was unsuccessful.

It is important to note that this re-orientation scheme introduces locally confined anisotropy. However, preliminary trials demonstrated that if instead a new starting position was generated after each detection of interpenetration, then the cylinder arrangement quickly became non-homogeneous due to the cylinders clustering near the boundaries of V as a result of the lower probability of interpenetration there. With the re-orientation scheme, no systematic errors were seen between theoretical and numerical results as a function of number of cylinders in a simulation (Overby, 2002), suggesting that any errors that might have been generated by this approach were not significant. Finally, V_V and S_V were computed as the sum for all cylinders of the volumes and surface areas, respectively, divided by V.

Many particle shapes are not well described by simple spheres or cylinders, most especially particles whose shape is not convex. To gain an idea of how successful the stereological

theory might be in predicting the projections of non-convex particles, we investigated arrangements of spherical and cylindrical particles where the particles were allowed to interpenetrate, thereby creating aggregates of particles that were not necessarily convex. Aggregates of interpenetrating spheres and cylinders were constructed using the same processes described above, only relaxing the conditions for non-interpenetration. Important for analysis of biological tissues, the interpenetrating cylinders produced using this method are architecturally similar to the fibrous scaffolding commonly observed within extracellular matrix resulting from the frequent cross-linking between neighbouring fibrous proteins.

For each arrangement of interpenetrating particles, the volume fraction V_V was determined by sampling a 3D grid of uniformly spaced points within V with a step size in each of the three coordinate directions of $0.25\mu_D$, or less. V_V was then determined as the fraction of points falling within the volume of any particle (Underwood, 1970). S_V was determined by counting the number of intersections of particles with vertical test lines along the 3D grid of points within V. Using the Saltykov relationship (Underwood, 1970), S_V was then computed from $2P_L$, where P_L is the number of intersections per unit length of the test lines. Convergence tests demonstrated that a grid step size of $0.25\mu_D$ is sufficient to calculate V_V and S_V within 4–6% of the theoretically approximated volume fraction and specific surface (Miles, 1976; Overby, 2002).

To compute the projected area and perimeter for a given depth-of-field t, a smaller rectangular test volume V_T of thickness t and area A_T was randomly selected within the larger volume V. The faces of V_T were parallel to the faces of V. To avoid the influence of edge effects that potentially arise from non-homogeneous particle distributions near the boundaries of V, a minimum distance, referred to as the boundary width, was defined between any face of V_T and the corresponding face of V. Convergence tests demonstrated that a boundary width of $10\times$ the mean sphere diameter or $2\times$ the mean cylinder length ($l = 10D$) was sufficient to eliminate edge effects in arrangements of spheres or cylinders (Overby, 2002). No special consideration was given to particles at the boundaries of V_T and truncation of particles by the edges of V_T was allowed, but only those portions of the particles contained within V_T were considered in the projected image.

For each particle contained at least partially within V_T, the total area and perimeter of each particle projected onto the plane of A_T were computed analytically and then discretized using at least ten points per unit diameter. A rectangular grid was used to discretize the projected area, while the projected perimeter was discretized using evenly spaced points along the perimeter boundary. The observed portion of the projected area and perimeter for each particle were computed from the fraction of discretized points that were observed on the projection multiplied by the analytical value of the projected area or perimeter. Each point was evaluated to determine if its vertical projection fell within the projection area A_T and if the point fell within the projected image of any another particle (i.e. overlap; see below). Discretization points that fell outside of the projection area A_T were not considered as observed. The discretization points were typically spaced at 10–20 points per mean particle diameter, and less than a 1% difference for either A'_A or L'_A occurred by changing the discretization length over this range (Overby, 2002).

The projected images from spheres having centroids lying outside of V_T that were intersected by either the upper or the lower surfaces of V_T were discretized using a circle of diameter $\sqrt{[(D/2)^2 - \zeta^2]}$, where ζ is the vertical distance between the centroid and the intersecting boundary. For right circular cylinders, the projected image appears as a rectangular central region flanked by two hemi-elliptical caps on opposite ends that arise from the projection of the cylinder's circular ends. One axis of each hemi-ellipse is orthogonal to the cylinder angle θ and its length is equal to the diameter of the cylinder, while the other axis depends upon the cylinder angle ψ and upon whether the cylinder is intersected by either surface (upper or lower) of V_T. Details describing the analytical determination of the shape and the discretization of these hemi-elliptical ends can be found in Overby (2002).

The observed fraction of the projected area and perimeter for each particle within V_T was determined by comparing the position of each discretized point with the projected area of all other particles and computing the number of points that were not contained within the projected area of any other particle (i.e. not-overlapped) and were contained within the projection plane, A_T. For the case of the projected area, the overlap condition was relaxed so that particles lying nearer to the lower surface of V_T would not be overlapped by particles lying nearer the upper surface of V_T (recall that the projected area of the lowest-lying particle is always observed on the projection plane, regardless of overlap). Finally, A'_A and L'_A were calculated by summing the observed portion of the projected area and perimeter for each contributing particle contained within V_T.

All computations were executed on a Dec-Alpha workstation using FORTRAN. The ISML routines *RNUNF* and *RNNOF* or exact functional equivalents were used to generate all uniformly distributed and normally distributed random numbers, respectively. For each parameter set investigated, at least five independent particle arrangements were analysed to produce the statistical results shown below, and all length scales were normalized by the mean diameter D; typical linear dimensions of V were 100-fold larger than D. For each particle shape, independent studies were conducted to verify that the numerical results were not sensitive to boundary effects caused by the absolute volume of V or to the discretization step-size. Further details can be found in the thesis by Overby (2002).

Results

To evaluate the stereological theory, we determined the projected area fraction A'_A and perimeter fraction L'_A as a function

of depth-of-field t for numerically generated random arrangements of non-interpenetrating spheres, cylinders or composite particle shapes made of interpenetrating spheres or cylinders. We then compared our numerical results with the predictions of the stereological theory. To simplify the presentation of data, we present A'_A and L'_A in terms of two dimensionless variables $(1 - A'_A)/(1 - V_V)$ and $4L'_A/(S_V\pi)$, respectively, that arise naturally in the theoretical analysis. These variables are expressed as functions of the dimensionless depth-of-field $\tau = tS_V/4(1 - V_V)$ for each arrangement. These results were then compared with the predictions of the dimensionless stereological equations (Eqs 7 and 11).

Generally, very good agreement was observed between the numerical results and the theoretical predictions, with predictions of A'_A tending to have smaller errors than did the predictions of L'_A. Both volume fraction and particle number density had little influence upon the agreement between the numerical results and theoretical predictions. Typically, the theoretical predictions for spheres were more accurate than for other particle shapes. The theory tended to be most accurate for depths-of-field (t) either much smaller than $4(1 - V_V)/S_V$ or much larger than this quantity, and generally the absolute difference between the results and theory was largest when τ was of order one.

Below are presented the results for the different particle shapes. In all figures, symbols represent the mean values of $(1 - A'_A)/(1 - V_V)$ or $4L'_A/(S_V\pi)$ determined from five independent particle realizations, while the error bars (usually smaller than the symbols) represent the standard deviation. Percentage error is defined as the difference between the numerically computed average value and the theoretical value (from Eq. 7 or Eq. 11) divided by the theoretical value. A more detailed account of the results, including those using the numerical model of interpenetrating polymer chains, the results of which were equally good, can be found in Overby (2002).

Non-interpenetrating spheres

Figure 4(A,B) show the numerical results of the projected dimensionless area fraction $(1 - A'_A)/(1 - V_V)$ and perimeter fraction $4L'_A/(S_V\pi)$ as a function of the dimensionless depth-of-field $\tau = tS_V/4(1 - V_V)$ for non-interpenetrating spheres of uniform diameter for varying volume fraction (V_V), where $V_V = 0.05$ (open circles), 0.10 (triangles) or 0.20 (squares), as well as results for spheres of normally distributed diameter ($V_V = 0.05$, $\sigma_D/\mu_D = 25\%$, filled circles).

As predicted by Eqs (7) and (11), the mean values of $(1 - A'_A)/(1 - V_V)$ all collapsed onto a single curve when plotted as a function of τ, while $4L'_A/(S_V\pi)$ was described by a family of curves that depended upon the value of β with $c = 1.5\pi$ (appropriate for spheres). Note that, using Eq. (13), $\beta = 4(1 - V_V)/cV_V$, and thus β is independent of S_V. Therefore, β is the same when comparing the cases of uniform and non-uniform sphere diameter with $V_V = 0.05$.

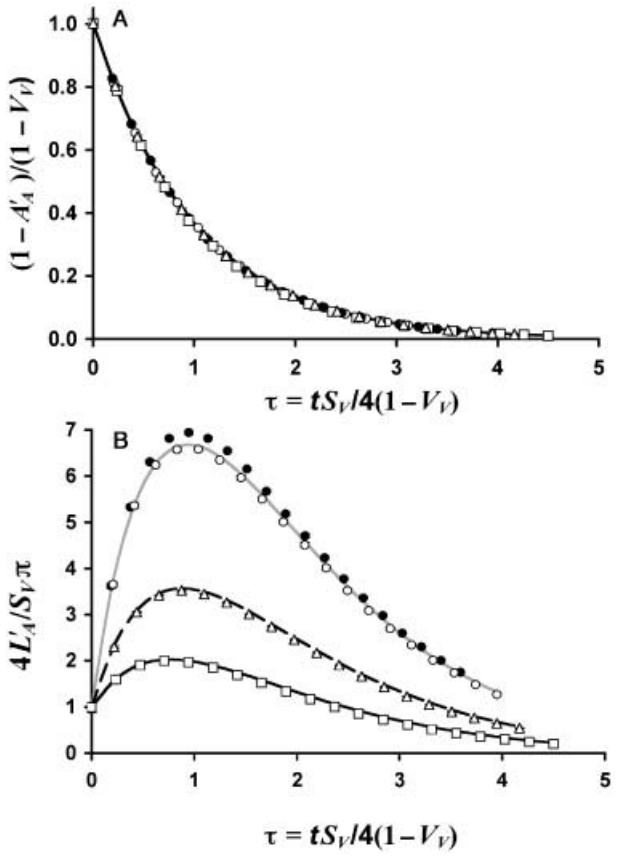

Fig. 4. Numerical measurements (symbols) and theoretical predictions (curves) of (A) the dimensionless void area fraction $(1 - A'_A)/(1 - V_V)$ and (B) the perimeter fraction $4L'_A/S_V\pi$ as a function of the dimensionless depth-of-field $\tau = tS_V/4(1 - V_V)$ for non-interpenetrating spheres of (i) uniform diameter D with $V_V = 0.05$, $S_V = 0.30D^{-1}$, $\beta = 16.1$ (open circles, grey curve in panel B); $V_V = 0.10$, $S_V = 0.60D^{-1}$, $\beta = 7.64$ (open triangles, dashed curve in panel B); and $V_V = 0.20$, $S_V = 1.20D^{-1}$, $\beta = 3.40$ (open squares, black curve in panel B), or (ii) non-uniform diameter where the diameter was varied according to a random normal distribution with $\sigma_D/\mu_D = 25\%$, $\mu_D = D$, $V_V = 0.05$, $S_V = 0.273D^{-1}$, $\beta = 16.1$ (filled circles, grey curve in panel B).

The numerical results for $(1 - A'_A)/(1 - V_V)$ shown in Fig. 4(A) exhibited excellent agreement with the theoretical predictions given by Eq. (7) throughout the entire range of τ and V_V investigated, with the error never exceeding 10%, even for the case of non-uniform sphere diameters. For $4L'_A/(S_V\pi)$ (Fig. 4B), the theoretical predictions for spheres of uniform diameter tended slightly to overestimate the numerical results, but the error was typically less than 10% and never exceeded 14%. The error for both $(1 - A'_A)/(1 - V_V)$ and $4L'_A/(S_V\pi)$ tended to increase for larger values of V_V and τ. By contrast, a normal distribution in sphere diameter ($\sigma_D/\mu_D = 25\%$) caused a theoretical under-prediction of the mean numerical values of $4L'_A/(S_V\pi)$ that peaked near 4% and was largest at about $\tau = 1$.

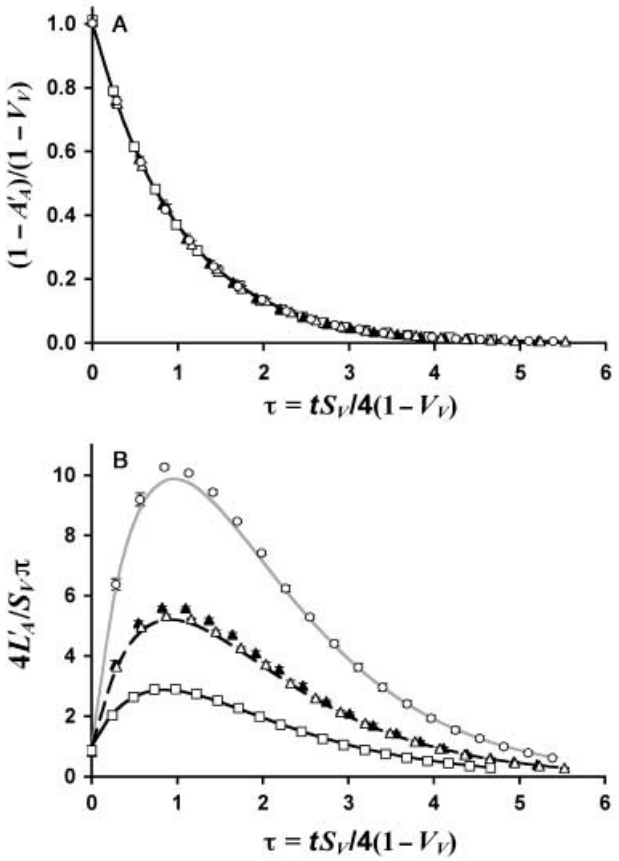

Fig. 5. Numerical measurements (symbols) and theoretical predictions (curves) of (A) $(1-A'_A)/(1-V_V)$ and (B) $4L'_A/S_V\pi$ as a function of $\tau = tS_V/4(1-V_V)$ for non-interpenetrating cylinders of (i) uniform diameter D and length $l = 10D$ with $V_V = 0.025$, $S_V = 0.105D^{-1}$, $\beta = 24.8$ (open circles, grey curve in panel B); $V_V = 0.05$, $S_V = 0.21D^{-1}$, $\beta = 12.1$ (open triangles, dashed curve in panel B); and $V_V = 0.10$, $S_V = 0.42D^{-1}$, $\beta = 5.73$ (open squares, black curve in panel B), or (ii) non-uniform diameter, but uniform length ($l = 10D$) where the cylinder diameter was varied according to a random normal distribution with $\sigma_D/\mu_D = 25\%$, $\mu_D = D$, $V_V = 0.05$, $S_V = 0.198D^{-1}$, $\beta = 12.1$ (filled triangles, dashed curve in panel B).

Non-interpenetrating cylinders

The predictions of the stereological theory were also in good agreement with the numerical results obtained from arrangements of non-interpenetrating cylinders for all volume fractions and for all cylinder lengths investigated, with somewhat larger errors for short cylinders ($l = 2D$). Figure 5(A,B) show results for cylinders of uniform diameter D and length $l = 10D$ where $V_V = 0.025$ (circles), $V_V = 0.05$ (open triangles) or $V_V = 0.10$ (squares), as well as results for cylinders of normally distributed diameter ($V_V = 0.05$, $\sigma_D/\mu_D = 25\%$, filled triangles). For all cases, $c = 2\pi$, as appropriate for infinitely long cylinders.

The mean measured values of $(1 - A'_A)/(1 - V_V)$ (Fig. 5A) collapsed onto a single exponential curve that was accurately predicted by Eq. (7), and the accuracy of this prediction was not significantly affected by changes in V_V or by a normally distributed cylinder diameter. For cylinders of uniform diameter, good agreement was also observed between the theoretical predictions and the numerical results for $4L'_A/(S_V\pi)$ (Fig. 5B), although a slight theoretical under-prediction was observed and was most pronounced for smaller values of V_V about $\tau = 1$; the error did not exceed 17%. This error arises from the approximation of c, and hence β, based upon infinitely long cylinders ($c = 2\pi$) that is applied to cylinders of finite length (compare with Eq. 14a). Supporting this point, the error in $4L'_A/(S_V\pi)$ became negligible (< 6%) for arrangements of longer cylinders with $l = 50D$, whereas more significant errors (up to 37%) were encountered when considering shorter cylinders with $l = 2D$ (Overby, 2002). Variability in cylinder diameter increased the magnitude of the theoretical under-prediction for $4L'_A/(S_V\pi)$, with the relative error approaching 9% near the peak about $\tau = 1$, compared with a 3% error observed for the uniform diameter case for the same values of τ and V_V. This error probably arises from the dependence of the average projected area, and hence $\overline{L'_2}$, upon second-order moments in D. By contrast, the accuracy of the theoretical predictions was fairly insensitive to distributions in cylinder length (Overby, 2002).

Interpenetrating spheres and cylinders

Randomly arranged convex particles that are allowed to interpenetrate form aggregate particles that can be viewed as non-convex, non-interpenetrating particles (instead of convex, interpenetrating particles). Thus, by constructing arrangements of interpenetrating convex particles, one may investigate the accuracy of the stereological theory for non-interpenetrating, non-convex geometries.

Figure 6(A,B) show the numerical results for $(1 - A'_A)/(1 - V_V)$ and $4L'_A/(S_V\pi)$ for interpenetrating arrangements of spheres (circles) or infinitely long cylinders (triangles) with $V_V = 0.05$ (open symbols) or $V_V = 0.10$ (filled symbols). For each arrangement, the constituent convex particles were of uniform size, and V_V and S_V for the non-convex aggregates were determined using numerical sampling routines that are described in the Methods section. Infinitely long interpenetrating cylinders were constructed using the same procedure described in the Methods section to construct arrangements of homogeneously distributed and isotropic cylinders, but the length of each cylinder was extended in both directions until the ends contacted the boundaries of V. Furthermore, because the cylinders are infinitely long, edge effects from the boundaries of V are negligible and, for this case, the boundary width was defined to be zero. The theoretical predictions represented by the curves in Fig. 6 were generated using the stereological theory for non-interpenetrating particles (Eqs 7 and 11), where $\beta = 4(1 - V_V)/cV_V$, and $c = 1.5\pi$ and $c = 2\pi$ for interpenetrating spheres or cylinders, respectively.

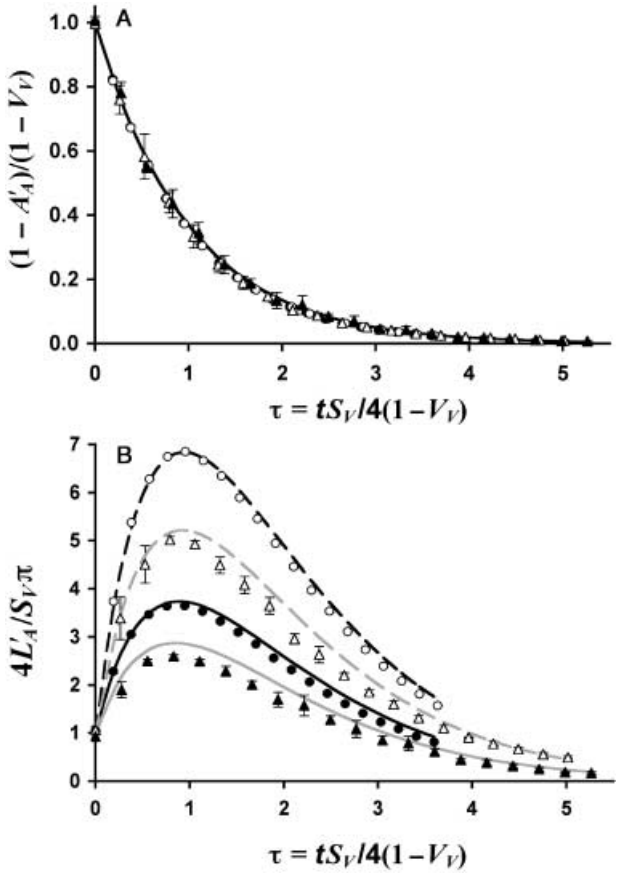

Fig. 6. Numerical measurements (symbols) and theoretical predictions (curves) of (A) $(1 - A'_A)/(1 - V_V)$ and (B) $4L'_A/S_V\pi$ as a function of $\tau = tS_V/4(1 - V_V)$ for (i) interpenetrating spheres with $V_V = 0.049$, $S_V = 0.28D^{-1}$, $\beta = 16.6$ (open circles, dashed curve in panel B) and $V_V = 0.095$, $S_V = 0.52D^{-1}$, $\beta = 8.09$ (filled circles, black curve in panel B) or (ii) interpenetrating infinitely long cylinders with $V_V = 0.05$, $S_V = 0.19D^{-1}$, $\beta = 12.1$ (open triangle, grey dashed curve in panel B) and $V_V = 0.10$, $S_V = 0.38D^{-1}$, $\beta = 5.73$ (filled triangles, grey curve in panel B). Spheres and cylinders were of uniform diameter and cylinders were infinitely long.

In general, the stereological theory for non-interpenetrating particles provided reasonably accurate predictions of the mean numerical values for both $(1 - A'_A)/(1 - V_V)$ and $4L'_A/(S_V\pi)$ for non-convex arrangements of either interpenetrating spheres or cylinders. The predictions for $(1 - A'_A)/(1 - V_V)$ were typically within 7% of the mean numerical values for interpenetrating spheres, but this difference was slightly larger (typically within 20%) for interpenetrating cylinders. By contrast, the predictions for $4L'_A/(S_V\pi)$ tended to overestimate the mean numerical values for both geometries, which was most pronounced about $\tau = 1$. The magnitude of the overestimation was larger for interpenetrating cylinders (2–20%) than for interpenetrating spheres (1–12%) and tended to increase for larger values of V_V.

Discussion

Current engineering and scientific analyses commonly focus upon structure and function at increasingly smaller length scales. Not surprisingly, electron microscopy has therefore emerged as an experimental standard to provide dimensional information at such small length scales. However, as these smaller scales are examined, intrinsic length scale effects, particularly those associated with the depth-of-field of the image being analysed, need to be considered to determine morphometric parameters accurately.

The depth-of-field of a micrograph refers to the thickness perpendicular to the projection plane that contributes to the observed image. This length scale is determined by several factors involved in the preparation of an electron microscopy image, including the focal depth of the electron beam, the thickness of the specimen that is being examined and, for samples prepared using the quick-freeze/deep-etch method, the coating and etching depth of the replica (Overby *et al.*, 2001). For transmission electron microscopy, the focal depth is typically larger than either the specimen thickness or the coating/etching depth, and the depth-of-field is thereby determined by the shorter of these parameters. By contrast, the focal depth for light microscopy is typically less than the specimen thickness so that out-of-focus structure often contributes to the projected image, confounding stereological analysis.

When the characteristic dimensions of relevant morphological features of a sample are of the same order of magnitude or smaller than the depth-of-field of a micrograph made from that sample, stereological corrections are necessary to characterize those features accurately using morphometric methods. We extended a stereological theory developed by Miles (1976) to account for depth-of-field effects and to allow the determination of the volume fraction (V_V) and specific surface (S_V) of a sample, from the 2D projected area fraction (A'_A) and perimeter fraction (L'_A) measured on a micrograph of that sample. Although we developed this theory to determine two specific 3D parameters (V_V and S_V), the theory should be relatively straightforward to generalize for determining other stereological parameters of interest.

Specifically, the stereological theory was developed for isotropic uniform random arrangements of non-interpenetrating or interpenetrating convex particles. By limiting the application of the theory to convex particle geometries including spheroids and cylinders (see Eq. 15), the stereological formulae reduce to explicit mathematical functions describing A'_A and L'_A in terms of V_V, S_V, t and a single geometric parameter (c) that is tightly bounded between 1.5π and 2π. With these assumptions, upper and lower bounds on V_V and S_V can be calculated by solving the stereological equations having measured A'_A and L'_A from a micrograph with c varying between the limits given by Eq. (15). The only additional information required to solve the stereological equations is the depth-of-field, for which standard measurement techniques exist, such

as direct measurement (Weibel, 1979) or parallax analysis of stereo image pairs (Nankivell, 1962; Underwood, 1970; Overby *et al.*, 2001).

To validate the stereological theory, numerical simulations were conducted to measure A'_A and L'_A as a function of depth-of-field for random arrangements of non-interpenetrating spheres or cylinders, or composite particles made of interpenetrating spheres or cylinders. The geometry of interpenetrating cylinders was introduced as an approximate model of the architecture generally found within extracellular matrix, which often includes cross-linked fibrous elements arranged in branching and anastomosing patterns (Hay, 1981). In general, the agreement between the theoretical predictions and numerical results was very good throughout the entire range of volume fraction and depth-of-field investigated. Theoretical agreement was best for non-interpenetrating spheres and cylinders with monodisperse diameter. Moreover, the success in predicting A'_A and L'_A for random arrangements of composite particles made of interpenetrating spheres or cylinders (which yield particles that are not-necessarily convex) suggests that the stereological theory for non-interpenetrating particles can be successfully applied towards some arrangements of non-convex particles, particularly those that are likely to be encountered in the extracellular matrix. This latter success may be partially due to the result that the stereological theory for non-interpenetrating particles yields an identical stereological relationship for A'_A to that given by Miles for interpenetrating particles (Eq. 6) (Miles, 1976; Stoyan *et al.*, 1987).

For non-monodisperse particle distributions, a somewhat appreciable error (~10%) was typically observed between the numerical results and theoretical predictions. This error can be nearly eliminated if the relationships describing $\overline{L'_2}$ [the characteristic size of a projected particle (Underwood, 1970)] are modified to reflect contributions from higher order moments in the distribution of the sphere or cylinder diameters (see Overby, 2002). This modification, however, typically eliminates any expression of $\overline{L'_2}$ in terms of only V_V and S_V (Eq. 13) and thereby prevents closure of the stereological relationships. Nevertheless, as Figs 4 and 5 demonstrate, approximating $\overline{L'_2}$ by Eqs (13) and (15) generally provides reliable estimates for A'_A and L'_A despite relatively large (25%) variations in particle diameter.

Our numerical validation studies were limited to relatively modest volume fractions ($V_V < 0.20$ for spheres and $V_V < 0.10$ for cylinders), owing to non-random arrangements that arise when higher solid fractions are numerically generated using random sequential addition. These non-random effects (non-stationary and non-isotropic distributions) can be especially important for cylindrical particle geometries, where excluded volume effects can introduce local anisotropy in fibre orientation. Although the volume fractions we investigated should be useful for many biological media, investigation of higher volume fractions would need to use alternative methods to generate stationary and isotropic particle distributions. Such distributions have be generated, for example, using germ-grain models with a hard core that employ progressive application of thinning rules (Stoyan & Schlather, 2000; Stoyan, 2000). However, such methods are difficult to apply for dense systems, and particularly for non-spherical particles (Stoyan, 2002).

Previous investigators have described stereological relationships between V_V and S_V, and their projected counterparts A'_A and L'_A (Underwood, 1970; Miles, 1976; Weibel, 1979, 1980; Stoyan *et al.*, 1987). Miles (1976), for instance, provided an accurate stereological theory to describe the influence of depth-of-field upon A'_A, L'_A and the projected curvature of L'_A per unit area. Miles' theory is valid for arrangements of interpenetrating convex particles, which can be equivalently interpreted as non-interpenetrating arrangements of not-necessarily convex particles. We developed a general formulation using a differential approach that allowed recovery of Miles' formulae for interpenetrating particles, but also allowed the theory to be extended to arrangements of non-interpenetrating particles. The stereological formulae for the projected area fraction, A'_A, is predicted to be identical for both non-interpenetrating and interpenetrating particle distributions (Eq. 7); however, different relationships are found for the projected perimeter fraction, L'_A (Eqs 11 and 12, respectively). The latter two equations become identical in the dilute limit, where $\beta \gg 1$, as would be expected.

For the stereological theory developed here, limiting geometrical assumptions (Eq. 15) were used to simplify the stereological formulae and obviate the need to measure the projected curvature, which is often a difficult measurement in practice (Weibel, 1979). These simplified stereological formulae express A'_A and L'_A as explicit mathematical functions of V_V, S_V, c and t. The advantage of this approach is that when these formulae are combined with the assumptions inherent in Eq. (15) and existing techniques to measure depth-of-field, one can calculate bounded estimates for V_V and S_V directly from measurements of A'_A and L'_A obtained from a single micrograph. Such an approach can also be combined with Miles' formulae to obtain simplified algebraic equations.

Application of the stereological formulae (Eqs 6, 10 and 13) in practice requires careful consideration of the assumptions underlying the stereological formulation. In the derivation of these formulae, we assume that the particles are randomly arranged and isotropically orientated, but such a distribution may or may not be accurately represented within the specimen of interest. Furthermore, assumptions of particle geometry limit the application to simple spheroidal and cylindrical shapes (Eq. 15); however, these limits are necessary to simplify the stereological formulae into tractable algebraic equations. The stereological theory accounts for the effects of overlap and overprojection caused by increasing depth-of-field, but it is important to recognize that other effects associated with increasing depth-of-field were not included in the current theory; such effects include decreased image resolution or

contrast and loss of particles at section boundaries due to particle capping (Cruz Orive, 1983). Deviations from these assumptions in practice would necessarily introduce inaccuracies in the stereological predictions, and the stereologist is therefore advised to evaluate these limiting assumptions carefully prior to application of the stereological formulae.

The current stereological theory was developed primarily to analyse the fibrous ultrastructure of extracellular matrix as seen using electron microscopy, particularly proteoglycans and basement membrane components, that may be modelled as arrangements of interpenetrating cylindrical fibres. The good agreement between the stereological theory and the numerical results for interpenetrating cylinder arrangements supports application of the theory toward nanometre-scale morphometric characterization of biological connective tissues (e.g. intracellular architecture and extracellular matrix) if these tissues can indeed be considered as isotropic uniform random arrangements of cylindrical fibres. Most biological connective tissues, however, exhibit anisotropy and have geometries outside the limits described by Eq. (15) that would limit application of our stereological theory. We recently used the stereological theory to analyse V_V and S_V of the interfibrillar matrix in corneal stroma, and used these results to estimate the specific hydraulic conductivity of this connective tissue. The results were in reasonable agreement with experimental measurements of this parameter (Overby *et al.*, 2001), supporting the use of this approach. However, the limitations and assumptions of the current theory should always be considered when modelling biological tissues.

In conclusion, the stereological technique was developed to determine morphometric parameters from projected images and is particularly suited towards the analysis of nanometre length-scale objects in electron micrographs, assuming isotropic uniform random arrangements of either interpenetrating or non-interpenetrating convex particles with simple spheroidal or cylindrical geometries. Most importantly, this stereological technique allows characterization of structural properties at these tiny length scales that are inaccessible by other direct measurement techniques. A general need for quantitatively accurate stereological assessments is exemplified by the application of stereology to fields as diverse as materials science (Karlsson & Cruz-Orive, 1992), anatomy (Weibel, 1967; Weibel & Paumgartner, 1978) and physiology (Ethier *et al.*, 1986; Levick, 1987; Overby *et al.*, 2001), and therefore it seems likely that the stereological theory developed in this report might be useful to a wide range of scientific disciplines.

Acknowledgements

We acknowledge support from the National Institutes of Health (EY09699 and EY14662), the American Health Assistance Foundation, the International Retinal Research Foundation and the many helpful suggestions of Drs Roger Kamm and William Deen of the Massachusetts Institute of Technology.

References

Abercrombie, M. (1946) Estimation of the nuclear population from microtome sections. *Anat. Rec.* **94**, 239–247.

Baddeley, A.J., Gundersen, H.J. & Cruz-Orive, L.M. (1986) Estimation of surface area from vertical sections. *J. Microsc.* **142**, 259–276.

Bolender, R., Paumgartner, D., Losa, G., Muellener, D. & Weibel, E. (1978) Integrated stereological and biochemical studies of hepatocytic membranes. I. Membrane recoveries in subcellular fractions. *J. Cell Biol.* **77**, 565–583.

Cruz-Orive, L.M. (1983) Distribution-free estimation of sphere size distributions from slabs showing overprojection and truncation, with a review of previous methods. *J. Microsc.* **131**, 265–290.

Cruz-Orive, L.M. (1997) Stereology of single objects. *J. Microsc.* **186**, 93–107.

Donev, A., Cisse, I., Sachs, D., Variano, E.A., Stillinger, F.H., Connelly, R., Torquato, S. & Chaikin, P.M. (2004) Improving the density of jammed disordered packings using ellipsoids. *Science*, **303**, 990–993.

Dubochet, J., Adrian, M., Chang, J., Homo, J., Lepault, J., McDowall, A. & Schultz, P. (1988) Cryo-electron microscopy of vitrified specimens. *Quart. Rev. Biophys.* **21**, 129–228.

Ethier, C.R. (1983) *Hydrodynamics of flow through gels with applications to the eye.* MS thesis, Massachusetts Institute of Technology, Cambridge, MA.

Ethier, C.R., Kamm, R.D., Palaszewski, B.A., Johnson, M. & Richardson, T.M. (1986) Calculations of flow resistance in the juxtacanalicular meshwork. *Invest. Ophthal. Vis. Sci.* **27**, 1741–1750.

Happel, J. & Brenner, H. (1983) *Low Reynolds Number Hydrodynamics*. Martinus-Nijhoff Publishers, The Hague.

Hay, E.D. (1981) *Cell Biology of Extracellular Matrix*. Plenum Press, New York.

Herczynski, R. (1975) Distribution function for random distribution of spheres. *Nature*, **255**, 540–541.

Hoang, Q., Linsenmeier, R., Chung, C. & Curcio, C. (2002) Photoreceptor inner segments in monkey and human retina: mitochondrial density, optics and regional variation. *Vis. Neurosci.* **19**, 395–407.

Karlsson, L. & Cruz-Orive, L. (1992) The new stereological tools in metallography: estimation of pore size and number in aluminum. *J. Microsc.* **165**, 391–415.

Långsjö, T.K., Hyttinen, M., Pelttari, A., Kiraly, K., Arokoski, J. & Helminen, H.J. (1999) Electron microscopic stereological study of collagen fibrils in bovine articular cartilage: volume and surface densities are best obtained indirectly (from length densities and diameters) using isotropic uniform random sampling. *J. Anat.* **195**, 281–293.

Levick, J.R. (1987) Flow through interstitium and other fibrous matrices. *Quart. J. Exp. Physiol.* **72**, 409–437.

Mack, C. (1956) On clumps formed when convex laminae or bodies are placed at random in two or three dimensions. *Proc. Cambridge Phil. Soc.* **52**, 246–250.

Miles, R.E. (1976) Estimating aggregate and overall characteristics from thick sections by transmission microscopy. *J. Microsc.* **107**, 227–233.

Miles, R.E. (1977) The importance of proper model specification in stereology. *Buffon Bicentenary Symposium on Geometrical Probability, Image Analysis, Mathematical Stereology, and Their Relevance to the Determination of Biological Structures* (ed. by R. E. Miles and J. Serra), pp. 115–136. Springer-Verlag, Paris.

Nankivell, J. (1962) Minimum differences in height detectable in electron stereomicroscopy. *Br. J. Appl. Physiol.* **13**, 126–128.

Ohser & Mücklich. (2000) *Statistical Analysis of Microstructures in Material Science*. Wiley, New York.

Overby, D. (2002) *The hydrodynamics of aqueous outflow*. PhD thesis, Massachusetts Institute of Technology, Cambridge, MA.

Overby, D., Ruberti, J., Gong, H., Freddo, T. & Johnson, M. (2001) Specific hydraulic conductivity of corneal stroma as seen by quick-freeze/deep-etch. *J. Biomech. Eng.* **123**, 154–161.

Satcher, R. & Dewey, C.F. (1996) Theoretical estimates of mechanical properties of endothelial cell cytoskeleton. *Biophys. J.* **71**, 109–118.

Satcher, R., Dewey, C. & Hartwig, J. (1997) Mechanical remodeling of the endothelial surface and actin cytoskeleton induced by fluid flow. *Microcirculation*, **4**, 439–453.

Stoyan, D. (2000) Basic ideas of spatial statistics. *Statistical Physics and Spatial Statistics* (ed. by K. R. Mecke and D. Stoyan), pp. 3–21. Springer, Berlin.

Stoyan, D. (2002) Simulation and characterization of random systems of hard particles. *Image Anal. Stereol.* **21**, S41–S48.

Stoyan, D., Kendall, W. & Mecke, J. (1987) *Stochastic Geometry and its Applications*. John Wiley & Sons, New York.

Stoyan, D. & Schlather, M. (2000) Random sequential adsorption: relationship to dead leaves and characterization of variability. *J. Statist. Phys.* **100**, 969–979.

Underwood, E.E. (1970) *Quantitative Stereology*. Addison-Wesley, Reading, MA.

Vouk, V. (1948) Projected area of convex bodies. *Nature*, **162**, 330–331.

Weibel, E. (1967) Introduction to stereology and morphometry. *Quantitative Methods in Morphology* (ed. by E. Weibel and H. Elias), pp. 2–19. Springer Verlag, Berlin.

Weibel, E.R. (1973) Morphological basis of alveolar-capillary gas exchange. *Physiol. Rev.* **53**, 419–495.

Weibel, E.R. (1979) *Stereological Methods: Practical Methods for Biological Morphology*. Academic Press, London.

Weibel, E.R. (1980) *Stereological Methods: Theoretical Foundations*. Academic Press, London.

Weibel, E. & Elias, H. (1967) Introduction of stereologic principles. *Quantitative Methods in Morphology* (ed. by E. Weibel and H. Elias), pp. 89–98. Springer Verlag, Berlin.

Weibel, E.R. & Gomez, D.M. (1962) A principle for counting tissue structures on random sections. *J. Appl. Physiol.* **17**, 343–348.

Weibel, E.R. & Paumgartner, D. (1978) Integrated stereological and biochemical studies on hepatocytic membranes. II. Correction of section thickness effect on volume and surface density estimates. *J. Cell Biol.* **77**, 584–597.

West, M.J., Slomianka, L. & Gundersen, H.J. (1991) Unbiased stereological estimation of the total number of neurons in the subdivisions of the rat hippocampus using the optical fractionator. *Anat. Rec.* **231**, 482–497.

Wicksell, S. (1925) The corpuscle problem: a mathematical study of a biometric problem. *Biometrica*, **17**, 84–99.